Poroelastic modeling of soap hole formation

Sarah Reid and Rachel Lauer

ABSTRACT

Soap holes were first identified >50 years ago as areas of localized surface weakness characterized by a thin and fragile crust covering sand, silt, clay, and water. It was hypothesized that they form where groundwater is moving upward to the ground surface through unconsolidated sediment. Soap holes are ubiquitous across the prairies and manifest as either mounds or flat exteriors underlain by liquefied mud. They range in diameter from less than 1-m to several meters and can reach up to several meters in depth. Due to their thin and fragile crust, they pose a risk to farming equipment and livestock, with several farmers reporting loss of cattle and extensive portions of land that are no longer farmable. Previous work has provided hydrological and geochemical constraints to create a conceptual model for soap hole formation. In this conceptual model, pressurized water from a confined aquifer travels upward through preferential flow paths in glacial till to a lacustrine deposit at the ground surface. There, the combined effects of increased fluid pressure and clay dispersion cause the soil to liquefy and form a soap hole. This study tests the conceptual model for soap hole formation by determining which parameters and processes impact the extent and volume of liquefaction in a 3-dimensional model using a steady state solution in COMSOL Multiphysics. In COMSOL, we employ Darcy's Law, solid mechanics, and poroelasticity to successfully approximate a simplified version of the observed field data. Variations in hydraulic, elastic, and geometric parameters were explored to determine their impact on the volume of liquefaction in the model. The results provide insight into the conditions required for soap hole formation, and serve to verify the conceptual model developed through field studies.

INTRODUCTION

Despite being ubiquitous across the Canadian Prairies and posing a significant risk to farming activities and equipment, there are few scientific studies of soap holes. The first reference to soap holes in the scientific literature is a 1966 study by Toth, who conducted a field survey mapping field phenomena in the central Alberta Plains. Toth (1966) describes soap holes as a geomorphic feature formed through groundwater discharge , and manifest as circular or elongated areas of localized weakness with a thin, fragile curst overlaying sand, silt, clay, and water (Toth, 1966; Toth, 1971). They can grow into mounds as tall as 2-m or be flat along the land surface, and can extend to several meters' depth. Several farmers have reported loss of cattle and farming equipment to soap holes, resulting in extensive regions of land that are no longer farmable. Figure 1 shows two soap holes located in the Alberta Prairie. Panel A displays a soap hole several meters in diameter with a farmer helping a cow out of a soap hole; Panel B shows a smaller, 1-m diameter soap hole.

FIG. 1. Two soap holes in Alberta. A. A farmer helps a cow that is stuck in a large soap hole. B. A small soap hole around 1 m in diameter.

Woods (2019) built on Toth's work by conducting the first major hydraulic, geophysical, and geochemical study of soap holes. The study included two field sites, named Rumsey and Torrington, each containing several soap holes. The hydraulic data revealed artesian flow conditions within the soap hole resulting in increased pore pressure at both field sites, and measurements outside the soap holes indicated downward flow (recharge) at Rumsey and variable flow at Torrington (Woods, 2019). At the field scale, the hydraulic conductivity values below the soap holes were 3 to 5 orders of magnitude larger than outside the soap hole, which led to the interpretation that there are high hydraulic conductivity lenses and fractures within the glacial till (Woods, 2019) that are potential fluid pathways. From the geochemical and geophysical data, Woods (2019) concluded that the soap hole mud formed from liquefaction of the surficial lacustrine material, and that the underlying artesian aquifers were the source of the water discharging from the soap holes. These data enabled Woods (2019) to develop the first conceptual model for soap hole formation. In this conceptual model, pressurized water from an artesian aquifer travels upward through preferential flow paths in glacial till to a lacustrine deposit at the ground surface. There, the combined effects of increased fluid pressure and clay dispersion cause the soil to liquefy and create a soap hole. Figure 2 illustrates the conceptual model for soap hole formation after Woods (2019).

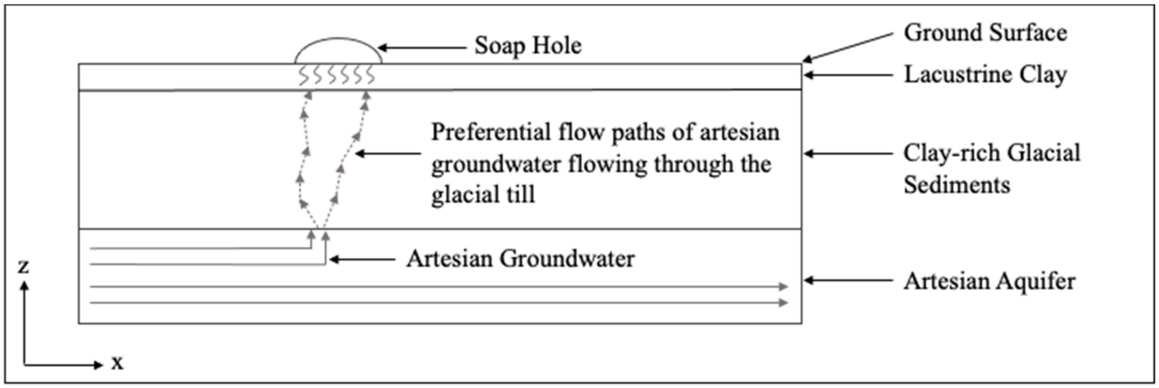

FIG. 2. The conceptual model for soap hole formation after Woods (2019). Artesian groundwater flows up from an aquifer through preferential flow paths in a clay-rich glacial till to the bottom of a lacustrine clay deposit. There, the combined effects of clay dispersion and an increased fluid pressure cause the sediment to liquefy and create a soap hole.

The objectives of this study are to test the conceptual model for soap hole formation and to determine which parameters and physical processes contribute to soap hole development. The objectives are achieved using a computer model developed in COMSOL Multiphysics (COMSOL, 1998-2019) to test several hypotheses:

1. Darcy's Law and poroelastic theory can accurately approximate the observed field phenomena,
2. The combination of high flow path permeability and low lacustrine deposit permeability are essential to soap hole formation,
3. Changes in elastic parameters will change the effective stress of the soil and extent of soap hole formation,
4. A flow path with high transmissivity will result in a larger volume soap hole, and
5. The thickness of the lacustrine deposit and glacial till above the pressurized aquifer will affect the extent of liquefaction and soap hole formation.

METHODS

Governing Equations

The governing equations for the model are a combination of fluid flow equations for saturated and unsaturated media, linearly elastic relationships between stress and strain, and poroelastic equations. Darcy's Law describes fluid flow through saturated material. COMSOL Multiphysics uses a pressure formulation of Darcy's Law, where fluid pressure is the dependent variable (COMSOL, 1998-2019). Adding a linearized storage model and the continuity equation to Darcy's Law gives the generalized equation for fluid flow (COMSOL, 1998-2019),

$$\rho_f S \frac{\partial p}{\partial t} + \nabla \cdot \rho_f \left[-\frac{\kappa}{\mu} \left(\nabla \mathrm{p} + \rho_f g \nabla D \right) \right] = Q_m, \tag{1}$$

where ρ_f is the fluid density (kg/m^3), S is the linearized storage model, p is the fluid pressure (Pa), t is time (s), κ is the permeability (m^2), μ is the dynamic viscosity of the fluid (Pa s), g is the gravitational constant (m/s^2), D is the elevation head (m), and Q_m is the mass source term (kg m^{-3} s^{-1}).

Richards' Equation and the van Genuchten Equations are used to describe fluid flow in variably saturated media. COMSOL Multiphysics uses a form of Richards' Equation that allows for time-dependent changes in saturated and unsaturated conditions (COMSOL, 1998-2019). However, if a stationary solver is used, then the time derivatives go to zero. The van Genuchten Equations define the variables in Richards' Equation, the relationship between fluid retention and permeability, and the fluid saturation when the fluid pressure is equal to atmospheric pressure (COMSOL, 1998-2019).

$$\rho_f \left(\frac{C_m}{\rho_f g} + Se\, S \right) \frac{\partial p}{\partial t} + \nabla \cdot \rho_f \left(-\frac{\kappa}{\mu} k_r (\nabla p + \rho g \nabla D) \right) = Q_m, \tag{2}$$

$$\theta = \begin{cases} \theta_r + Se(\theta_s - \theta_r), \; H_p < 0 \\ \theta_s, \; H_p \geq 0' \end{cases} \tag{3}$$

$$Se = \begin{cases} \frac{1}{\left[1+|\alpha H_p|^n\right]^m}, \; H_p < 0 \\ 1, \; H_p \geq 0 \end{cases}, \tag{4}$$

$$C_m = \begin{cases} \frac{\alpha m}{1-m}(\theta_s - \theta_r) Se^{\frac{1}{m}}\left(1 - Se^{\frac{1}{m}}\right)^m, \; H_p < 0 \\ 0, \; H_p \geq 0 \end{cases}, \tag{5}$$

$$k_r = \begin{cases} Se^l\left[1 - \left(1 - Se^{\frac{1}{m}}\right)^m\right]^2, \; H_p < 0 \\ 1, \; H_p \geq 0 \end{cases}, \tag{6}$$

where C_m is the specific moisture capacity, Se is the effective saturation, k_r is the relative permeability (m^2), θ is the volume of liquid per porous medium volume, θ_r is the residual volume fraction, θ_s is the saturated volume fraction, H_p is the pressure head (m), and α, n, m, l are constants for a particular material type.

Assuming the model is composed of a homogeneous, isotropic, and linearly elastic material, the relationship between stress and strain is (Krebes, 2019),

$$\sigma_{ij} = \sum_{k=1}^{3}\sum_{l=1}^{3} c_{ijkl}e_{kl}, \qquad i,j = 1,2,3, \tag{7}$$

where σ_{ij} is the stress tensor, c_{ijkl} is the stiffness tensor, and e_{kl} is the strain tensor. If the stiffness tensor is written in terms of Young's Modulus and Poisson's Ratio, it becomes (COMSOL, 1998-2019),

$$c_{ijkl} = \frac{E}{(1+\nu)(1-2\nu)}\begin{bmatrix} 1-\nu & \nu & 0 & 0 & 0 & 0 \\ \nu & 1-\nu & 0 & 0 & 0 & 0 \\ \nu & \nu & 1-\nu & 0 & 0 & 0 \\ 0 & 0 & 0 & \frac{1-2\nu}{2} & 0 & 0 \\ 0 & 0 & 0 & 0 & \frac{1-2\nu}{2} & 0 \\ 0 & 0 & 0 & 0 & 0 & \frac{1-2\nu}{2} \end{bmatrix}, \tag{8}$$

where E is Young's Modulus (Pa), and ν is Poisson's Ratio.

COMSOL Multiphysics couples fluid flow and solid mechanics using poroelasticity, where fluid pressure is the dependent variable and the coupling term (COMSOL, 1998-2019). The mass conservation equation after incorporating poroelasticity becomes,

$$\rho_f S \frac{\partial p_f}{\partial t} + \nabla \cdot \left(\rho_f \vec{u}\right) = -\rho_f \alpha_B \frac{\partial}{\partial t} e_{vol}, \tag{9}$$

where α_B is the Biot-Willis Coefficient, and e_{vol} is the volumetric strain. The Stationary Solver in COMSOL Multiphysics solves this equation by removing the time derivatives (COMSOL, 1998-2019).

To quantify soap hole formation, the effective stress within the model is examined. When a normal force is applied over an area of material, the force is resisted by the grain-to-grain contact of the sediment and by the pore water (Knappet, et al., 2020). The effective stress describes the amount of the applied force that is supported by the grain-to-grain contact (or solid skeleton). If the pore pressure increases and the force is primarily resisted by the pore water instead of the solid skeleton, the grain-to-grain contact of the sediment decreases and the effective stress approaches zero. An effective stress of zero is indicative of liquefaction in soils and unconsolidated sediment. COMSOL Multiphysics computes the effective stress as,

$$\sigma'_{ij} = c_{ijkl} e_{kl} - \alpha_B p \delta_{ij}. \tag{10}$$

Model Domain

The model requires several physical, hydraulic, and geometric parameters, many of which are well constrained by the field data collected by Woods (2019), Shatar (2020), and Cunningham (in progress). Parameters that are unconstrained by the field data are collected from literature for a range of values for lacustrine deposits and glacial till in Alberta (Elwood and Martin, 2010; Eisenstein and Thomson, 1977; Eisenstein and Morrison, 1972; Wang, et al., 2012; Burgess and Eisenstein, 1977; Hamilton, 1966; Grisak and Cherry, 1975; Morgan, 2019; van Genuchten, 1980; Wosten and van Genuchten, 1988; Carsel and Parish, 1988; Jalilzadeh, 2019). An initial model is created and compared to the field data to determine the model's accuracy in recreating the observed field phenomena.

The geometry and boundary conditions of the model are displayed in Figure 3. The 3-dimensional model consists of a volume 100 m by 100 m by 12 m in the x-, y-, and z-directions, respectively. The top 2 m of the model is defined as the lacustrine deposit, and the bottom 10 m is defined as the glacial till. A fracture of 2 cm by 2 cm by 10 m in the x-, y-, and z-directions, respectively, extends from the base of the model up to the interface between the lacustrine deposit and the glacial till. Fluid flow in the lacustrine deposit is governed by Richards' Equation for variably saturated media, and the rest of the model is governed by Darcy's Law. The material parameters assigned to the model are collected in Table 1.

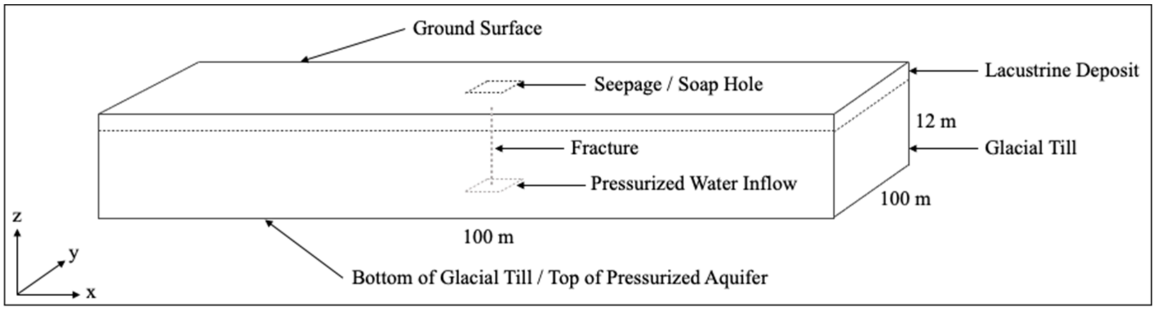

FIG 3. The geometry and boundary conditions of the 3-dimensional model.

The initial conditions assigned to the model include a fluid pressure equal to atmospheric pressure across the entire domain and displacement and structural velocity fields set to zero in all directions. The fluid pressure can then increase as the model incorporates gravity and reaches hydrostatic conditions, and there is no initial force acting on the domain. The bottom of the boundary is assigned a rigid boundary condition where the displacement is zero in all directions (COMSOL, 1998-2019). It is also assigned a no flow condition, apart from a 4 m by 4 m square in the middle of the boundary. This square is assigned a fluid pressure equal to the pressure of the underlying aquifer. The aquifer pressure is calculated by extrapolating the hydraulic head data from Rumsey and Torrington (Woods, 2019) down to the depth of the aquifer. The top boundary of the model is assigned a free displacement condition, where the displacements can occur freely in any direction (COMSOL, 1998-2019). The fluid flow conditions for the top boundary are like those for the bottom boundary. The top boundary of the domain is a no flow boundary, with a 4 m by 4m square in the middle. The square is assigned a pressure equal to atmospheric pressure. Seepage can then occur out of the top of the model, mimicking a soap hole and establishing consistency with field observations. A roller boundary is assigned to the sides of the model domain, so the model grid can "roll" vertically along the boundary, but it may not extend perpendicular to the boundary (COMSOL, 1998-2019). The sides of the model are assigned a hydrostatic boundary condition using the water table elevation from the Rumsey and Torrington field sites as a reference (Woods, 2019).

A tetrahedral mesh was selected using the built-in physics-controlled meshing option in COMSOL Multiphysics. The physics-controlled mesh is adapted to the physics already applied to the model (COMSOL, 1998-2019). The extremely fine element option is selected to resolve the fracture, with the element sizes ranging from 0.02 m to 2 m. The maximum element growth rate is 1.3, and the resolution of narrow regions is 1 element since the narrowest region is along the fracture, which can be resolved by the smallest element size.

Table 1. The hydraulic, physical, and geometric parameters assigned to the lacustrine deposit, glacial till, and fracture in the base model. S_s: specific storage, K: hydraulic conductivity, E: Young's Modulus, ν: Poisson's Ratio, ρ: material density, α_B: Biot-Willis Coefficient, n: porosity.

Parameter	Lacustrine Deposit	Glacial Till	Fracture
S_s (1/m)	2e-2	1e-2	4.5e-4
K (m/s) *	1e-11	1e-10	1e-6
E (MPa)	75	200	200
ν	0.45	0.35	0.35
ρ (kg/m^3) *	1200	1800	1800
α_B	1	0.5	0.7
n *	0.6	0.5	0.7
Thickness (m)	2 *	10	

Sensitivity Analysis

The model sensitivity is analyzed to examine which parameters affect the model results. A range of possible values for each parameter and material were collected from the field data, or literature review if no field data were available. The sensitivity analysis includes variations in hydraulic, elastic, and geometric parameters, and Table 2 includes the minimum and maximum values for each parameter. The volume of liquefaction is calculated for each simulation to determine the sensitivity of soap hole formation to each parameter. It is calculated by taking a vertical cross section through the model and fitting a polygon to the datapoints where the effective stress is less than or equal to zero. The volume is then calculated from the polygon assuming an axially symmetric volume of liquefaction.

Table 2. The hydraulic, elastic, and geometric parameters for the lacustrine deposit, glacial till, and fracture in the base model and the range of values for the sensitivity analysis. S_s: specific storage, K: hydraulic conductivity, E: Young's Modulus, ν: Poisson's Ratio, ρ: material density, α_B: Biot-Willis Coefficient, n: porosity, α *: van Genuchten constant, n*: van Genuchten constant, θ_s: saturated fluid fraction, θ_r: residual fluid fraction.

Parameter	Lacustrine Deposit			Glacial Till			Fracture		
	Base	Min	Max	Base	Min	Max	Base	Min	Max
S_s (1/m)	2e-2	1.5e-2	2.5e-2	1e-2	2e-3	5e-3	4.5e-4	4e-4	5e-3
K (m/s)	1e-11	5e-12	5e-10	1e-10	2.5e-11	2e-9	1e-6	1.5e-8	1e-5
E (MPa)	75	40	100	200	20	350	200	20	350
ν	0.45	0.45	0.45	0.35	0.3	0.4	0.35	0.3	0.4
ρ (kg/m^3)	1200	1100	1500	1800	1500	2300	1800	1500	2300
n	0.6	0.4	0.9	0.5	0.37	0.59	0.7	0.5	0.8
Thickness or Length (m)	2	2	4	10	1	45	10	1	45
α (1/m)*	1	0.5	14	-	-	-	-	-	-
n*	2	1.08	2.5	-	-	-	-	-	-
θ_s *	0.45	0.4	0.5	-	-	-	-	-	-
θ_r *	0.05	0.01	0.2	-	-	-	-	-	-
Aperture (m)	-	-	-	-	-	-	0.02	0.02	1
Aquifer potentiometric surface (mags)	-	-	-	3	0	4	-	-	-

RESULTS

Base Model

The mass balance for the base model is calculated by summing the inflow and outflow fluxes, where fluxes are positive for outflow (COMSOL, 1998-2019). The inflow boundaries in this study include only the small square on the bottom boundary of the model domain. The inflow flux is -1.365E-2 kg/h. The outflow flux is calculated from the small square on the top boundary and from the sides of the model domain. The outflow is 1.365E-2 kg/h, and the mass flow difference between inflow and outflow is -1.8E-7 kg/h. The resulting error of mass balance is 0.001318% and is accepted to be a reasonable error for this study.

The effective stress and hydraulic head results from the base model are plotted in Figure 4. Panel A is a vertical cross section of the middle of the model at y = 50 m and intersects the fracture in the middle of the model domain. The plot is contoured for effective stress, where black is high effective stress and white is low effective stress. Areas of high effective stress are concentrated at the bottom of the cross section, and the effective stress decreases as the elevation increases toward the ground surface. There is also a drop in effective stress at 50 m distance relative to the surrounding effective stress at the same elevations. The white contour at the top center of the cross section indicates an area of effective stress less than or equal to zero. This contour occurs in the top 2 m of the cross section at surface distances of 40 m to 60 m and decreases in a pseudo-triangular shape to approximately 840 m elevation.

The base model results are compared to the field data for Rumsey and Torrington in Figure 4 Panels B and C. Two cut lines are selected from the cross section in Panel A at 50 m and 70 m distance. 50 m is equivalent to data collected within and below the soap hole (solid black line), and 70 m is equivalent to outside the soap hole (dashed black line) and offers a background comparison. The effective stress calculated within and outside the soap hole is plotted in Panel B. The upper and lower limits of the field data are colored with a light grey polygon. At 50 m distance, the effective stress from the model falls within the range of the effective stress in the field, and the model results follow a similar trend as the field data, where there is a change in slope at the lacustrine-glacial till interface at 840 m elevation. However, the effective stress at 70 m does not fall within the bounds of the effective stress from the field data outside the soap hole. The model underestimates the background effective stress and remains above zero as the elevation increases. There is also more variability in the field data compared to the model results at 70 m. The hydraulic head from the model is compared to the field observations in Panel C. Within the soap hole, the hydraulic head in the model follows a similar trend as the field sites, where the hydraulic head increases with depth indicating an upward fluid flow. The hydraulic head trend in the model has a change in slope at 840 m elevation at the lacustrine-glacial till interface. The same change in slope is not observed in the field data. Outside the soap hole, the hydraulic head in the model is constant with depth and is larger than the field data. Furthermore, the hydraulic head at Rumsey indicates downward flow, and the hydraulic head at Torrington indicates variable flow.

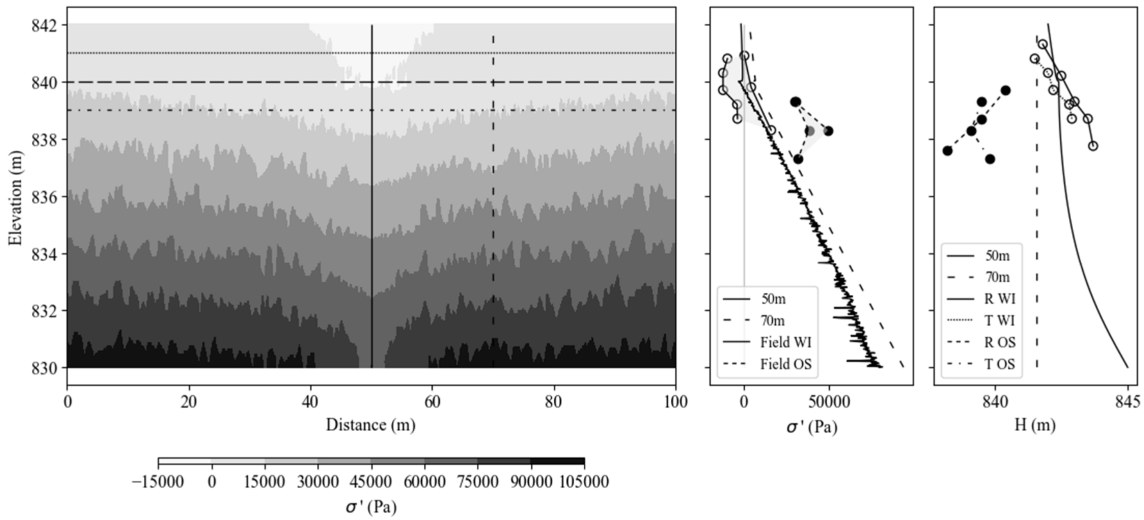

FIG. 4. The base model results. A. A vertical cross section of the 3D model taken at y = 50 m. It is contoured for effective stress. The vertical solid and dashed black lines represent the locations of the solid and dashed black lines plotted in B and C. B. The effective stress from vertical cut lines at x = 50 m and x = 70 m plotted with the effective stress from Rumsey and Torrington field sites. The light grey polygons indicate the range of values at the field sites. WI: within soap hole. OS: outside soap hole. C. The hydraulic head at the same vertical cut lines at x = 50 m and x = 70 m plotted with the hydraulic head observed at the Rumsey and Torrington field sites. R WI: Rumsey within soap hole. T WI: Torrington within soap hole. R OS: Rumsey outside soap hole. T OS: Torrington outside soap hole.

Sensitivity Analysis

Soap hole formation is quantified by the volume of liquefaction in the model, and the percent change in the values is calculated to determine if the model is sensitive to variations in that parameter. For example, as the lacustrine deposit hydraulic conductivity varies, the resulting values of the volume of liquefaction are collected. The minimum and maximum volumes of liquefaction are determined from the set of lacustrine hydraulic conductivity values, and the percent change is calculated.

$$percent\ change = \frac{max - min}{max + min} \times 100\% . \tag{11}$$

The calculated percent change for each parameter and material are collected in Table 3. Values above 1% indicate that the volume of liquefaction in the model is sensitive to variations in that parameter. Using the cutoff of 1%, the volume of liquefaction is sensitive to changes in hydraulic conductivity, Young's Modulus, Poisson's Ratio, density, Biot-Willis Coefficient, unit thickness, fracture width, and aquifer pressure.

Table 3. Percent change of the volume of liquefaction for the range of value for each parameter assigned to the lacustrine deposit, glacial till, and fracture. Bolded items indicate a percent change greater than 1%. * indicates parameters used in the van Genuchten and saturation functions. S_s: specific storage, K: hydraulic conductivity, E: Young's Modulus, ν: Poisson's Ratio, ρ: material density, α_B: Biot-Willis Coefficient, n: porosity, α *: van Genuchten constant, n*: van Genuchten constant, θ_s: saturated fluid fraction, θ_r: residual fluid fraction.

Parameter	**Percent change (%)**		
	Lacustrine	Glacial Till	Fracture
S_s	0.00	0.00	0.00
K	**81**	**6.4**	**47**
E	**7.5**	**36**	0.00
ν	-	**3.4**	0.00
ρ	**75**	**3.3**	0.00
α_B, n	0.043	**21**	0.00
Thickness	**40**	**59, 100**	-
α *		0.00	
n *		0.00	
θ_s *		0.00	
θ_r *		0.00	
Fracture Aperture		**57**	
Aquifer potentiometric surface		**99**	

The model is sensitive to change in hydraulic conductivity for all three materials. In Figure 5 Panel A, the volume of liquefaction decreases from 35.2 m^3 to 3.76 m^3 as the lacustrine hydraulic conductivity increases from 5E-12 m/s to 5E-10 m/s. Similarly, the volume of liquefaction decreases from 38.4 m^3 to 33.7 m^3 as the glacial till hydraulic conductivity increases from 2.5E-11 m/s to 2E-9 m/s. However, the volume of liquefaction increases from 21.2 m^3 to 58.5 m^3 as the fracture hydraulic conductivity increases from 1.5E-8 m/s to 1E-5 m/s. The largest change in volume of liquefaction occurs when changing the fracture hydraulic conductivity. There is an increase of 37.3 m^3, compared to decreases of 31.4 m^3 and 4.7 m^3 for variable lacustrine and glacial till hydraulic conductivities, respectively.

The ratios between the hydraulic conductivity for each material type are plotted in Figure 5 Panels B-D. As the ratio of fracture hydraulic conductivity to glacial hydraulic conductivity increases from 150 to 100,000, the volume of liquefaction also increases from 11.5 m^3 to 37.2 m^3. In Panel C, as the ratio of the fracture hydraulic conductivity to the lacustrine hydraulic conductivity increases from 1,500 to 1,000,000, the volume of liquefaction increases from 30.1 m^3 to 58.5 m^3. In Panel D, as the ratio of glacial hydraulic conductivity to lacustrine hydraulic conductivity increases from <1 to 200, there is a large initial jump in volume of liquefaction, which then levels off when the ratio approaches 10.

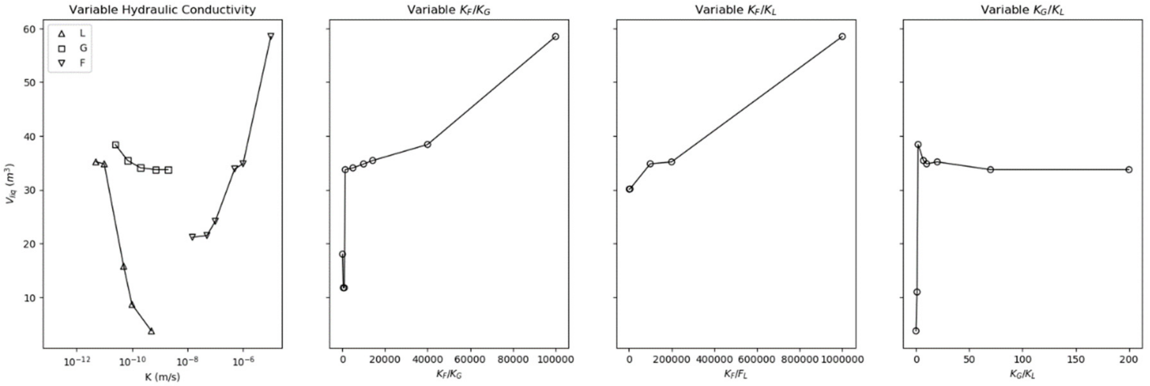

FIG. 5. The volume of liquefaction for, A. variations in lacustrine hydraulic conductivity (Δ), variations in glacial till hydraulic conductivity (⊡), and variations in fracture hydraulic conductivity (∇), B. variations in the ratio of the fracture hydraulic conductivity to the glacial till hydraulic conductivity, C. variations in the ratio of the fracture hydraulic conductivity to the lacustrine deposit hydraulic conductivity, and D. variations in the ratio of the glacial till hydraulic conductivity to the lacustrine deposit hydraulic conductivity.

The model is also sensitive to variations in Young's Modulus, Poisson's Ratio, density, and the Biot-Willis coefficient in some of the materials. In Figure 6 Panel A, As the lacustrine Young's Modulus increases from 40 MPa to 100 MPa, the volume of liquefaction also increases slightly from 20.5 m^3 to 23.9 m^3. However, as the glacial till Young's Modulus increases from 20 MPa to 350 MPa, the volume of liquefaction decreases from 68.5 m^3 to 32.1 m^3. In Figure 6 Panel B, as the glacial till Poisson's Ratio increases from 0.30 to 0.40, the volume of liquefaction decreases slightly from 35.9 m^3 to 33.5 m^3. There is a large change in volume of liquefaction for variations in the lacustrine density in Panel C. As the lacustrine density increases from 1100 kg/m^3 to 1500 kg/m^3, the volume of liquefaction decreases from 59.1 m^3 to 9.36 m^3. As the glacial density increases from 1500 kg/m^3 to 2300 kg/m^3, the volume of liquefaction steadily decreases from 36.0 m^3 to 33.5 m^3. The Biot-Willis coefficient for the glacial till and fracture are equal to the porosity, and as the Biot-Willis coefficient is changed so is the porosity. As the glacial Biot-Willis coefficient increases from 0.37 to 0.59, the volume of liquefaction increases from 30.6 m^3 to 46.7 m^3 in Panel D.

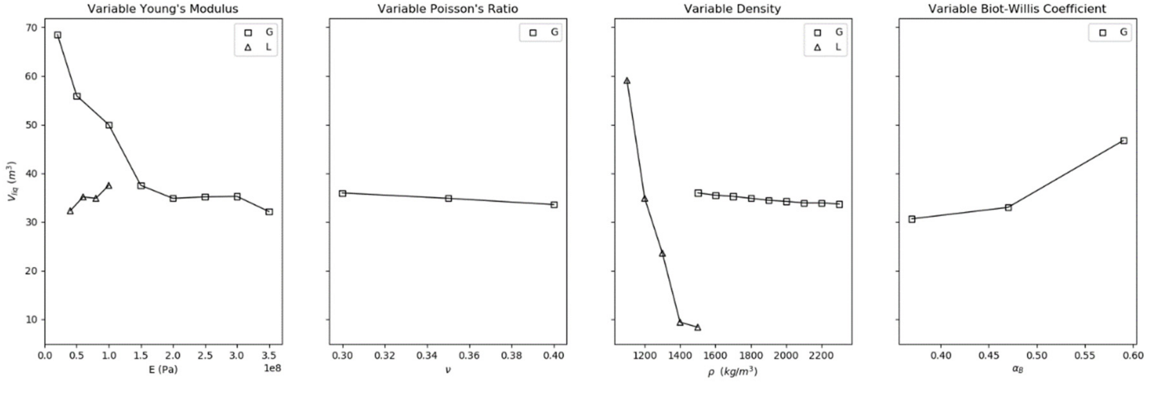

FIG. 6. The volume of liquefaction for, A. variations in the glacial till and lacustrine deposit Young's Moduli, B. variations in the glacial till Poisson's Ratio, C. variations in the glacial till and lacustrine densities, and D. variations in the glacial till Biot-Willis Coefficient.

The model is sensitive to the thickness of the lacustrine deposit and glacial till units, the width or aperture of the fracture, and the aquifer pressure. In Figure 7 Panel A, as the glacial till thickness increases from 1 m to 10 m with a fracture width of 0.02 m, the volume of liquefaction decreases from 174.4 m^3 to 34.8 m^3. Similarly, as the glacial till thickness increases from 15 m to 45 m with a fracture width of 0.1 m, the volume of liquefaction decreases from 41.8 m^3 to 0.031 m^3 and levels off at a thickness of 30 m. There is a very small decrease in volume of liquefaction as the lacustrine thickness increases from 1 to 4 m thick. In Panel B, as the fracture width increases from 0.02 m to 1 m, the volume of liquefaction increases from 34.8 m^3 to 108.1 m^3. The aquifer pressure is assigned to the bottom model square as a potentiometric surface in meters above the ground surface. As the potentiometric surface increases from 1 mags to 4 mags, the volume of liquefaction increases from 0.599 m^3 to 56.8 m^3 in Panel D.

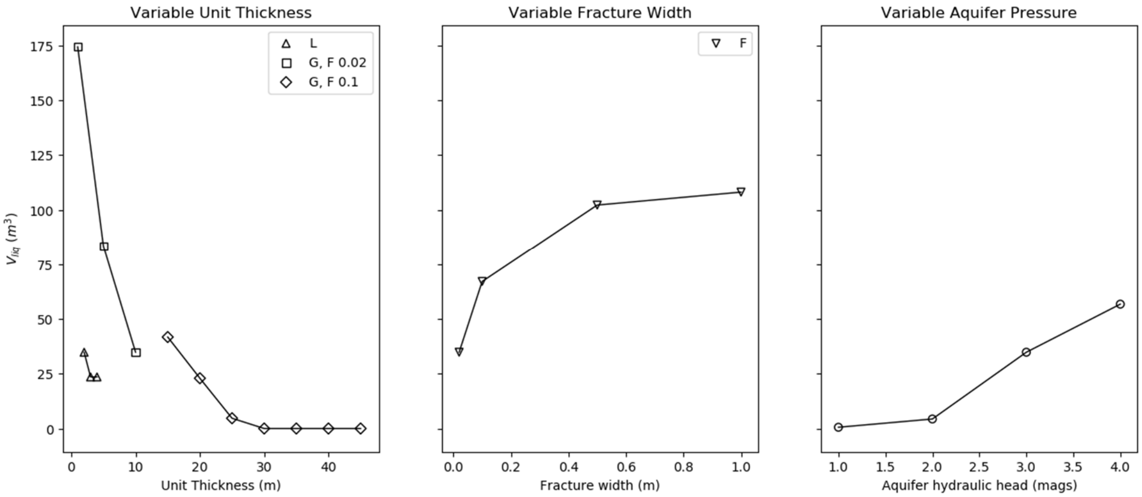

FIG. 7. The volume of liquefaction for, A. variations in lacustrine thickness, glacial till thickness with a 0.02 m wide fracture, and glacial till thickness with a 0.1 m wide fracture, B. variations in the fracture width, and C. variations in the aquifer potentiometric surface.

DISCUSSION

Base Model

In a vertical cross section like the one in Figure 4 Panel A, the effective stress increases with depth due to the body force exerted by the material above. As the thickness of the material increases, the total body force exerted on the material below increases resulting in a corresponding increase in stress. For hydrostatic unconfined boundary conditions, there is no excess fluid pressure for an increase in applied force. Therefore, there is no change in the amount of force that is supported by the pore pressure. The force is primarily resisted by the grain-to-grain contact, and the effective stress increases with depth. The decrease in effective stress at x = 50 m along the cross section is due to an increase in fluid pressure at the center of the model. The inflow boundary is located at 48 m to 52 m along the base of the cross section, and the fluid pressure translates up through the fracture resulting in a decrease in effective stress at the center of the cross section relative to the surrounding material.

The white contour in Figure 4 Panel A represents the area of liquefaction in the model. The liquefaction is concentrated within the lacustrine deposit due to different hydraulic and physical parameters than the glacial till. Compared to the glacial till and fracture, the lacustrine deposit has the lowest hydraulic conductivity, the lowest Young's Modulus, the largest Poisson's Ratio, and the largest Biot-Willis coefficient. A small Young's Modulus indicates that a small amount of stress will result in a large amount of strain in the material, and a large Young's Modulus indicates the opposite: that a large amount of applied stress is required to produce the same amount of strain. The smaller Young's Modulus of the lacustrine deposit then suggests that a smaller amount of stress is needed to result in strain (or deformation) compared to the glacial till and fracture. The larger Poisson's Ratio of the lacustrine deposit also indicates that the material experiences more strain perpendicular to the applied force when compared to a smaller Poisson's Ratio. The relative magnitude of these parameters together mean that the low hydraulic conductivity prevents fluid from moving as easily through the lacustrine deposit, and the fluid pressure builds in a material that will experience more strain relative to the glacial till and fracture for the same amount of applied force. A larger Biot-Willis Coefficient means that the fluid pressure holds a greater weight on the calculation for effective stress, and the effective stress will decrease as the Biot-Willis Coefficient increases for a constant pore pressure.

While the effective stress at 50 m distance along the cross section falls within the range of field values, the effective stress at 70 m distance and the hydraulic head do not align perfectly with the field observations. A major assumption for the model is that each of the materials are homogeneous, isotropic, and linearly elastic. This results in a simplified model compared to the field, where these assumptions would not hold. The heterogeneity of glacial till would result in variations in hydraulic conductivity in the subsurface, which may explain the variations in the hydraulic head from the field data. The model would require more complexity in the glacial till to reproduce the observed field phenomena.

Sensitivity Analysis

The trends in Figure 5 represent fluid flow and pressure buildup for a variety of hydraulic conductivity scenarios. As the lacustrine hydraulic conductivity increases, fluid from the fracture moves more easily through the lacustrine deposit to the ground surface where it can exit the system. This process decreases the fluid pressure buildup within the lacustrine deposit, thereby decreasing the volume of liquefaction. As the glacial till hydraulic conductivity increases, fluid escapes from the fracture into the surrounding glacial till more easily. The fluid pressure at the top of the fracture then decreases, resulting in a decrease of fluid pressure within the lacustrine deposit and a decrease in the volume of liquefaction. As the fracture hydraulic conductivity increases, fluid moves through the fracture with ease until the lacustrine-glacial till interface. More fluid pressure is translated through the fracture, resulting in a larger fluid pressure at the interface and a larger volume of liquefaction within the lacustrine deposit. The volume of liquefaction increases for increases in the K_F/K_G and K_F/K_L ratios. Large values in K_F/K_G occur for large fracture hydraulic conductivities and low glacial till hydraulic conductivities. In that scenario, fluid is more confined to within the fracture resulting in more fluid pressure translated up through the fracture. The increase in fluid pressure at the interface once again results in an increase in the volume of liquefaction within the lacustrine deposit. Large values in K_F/K_L occur when the fracture hydraulic conductivity is significantly larger than the lacustrine deposit hydraulic conductivity. The fluid pressure is easily translated up through the fracture but is unable to pass as easily through the lacustrine deposit to the seepage boundary. This scenario results in an increase in fluid pressure within the lacustrine deposit and increases the volume of liquefaction. The initial jump in the volume of liquefaction for small values of K_G/K_L demonstrates the importance of a confining layer for soap hole formation. Small values of K_G/K_L occur when the lacustrine hydraulic conductivity is greater than or equal to the glacial till hydraulic conductivity, which represents a lack of confining layer and a small volume of liquefaction. The confining layer allows fluid pressure to build to decrease the effective stress enough to create a soap hole.

In Figure 6 Panel A, the volume of liquefaction decreases as the glacial till Young's Modulus increases. Hicher (1996) and Casey et al. (2016) showed that Young's Modulus of a material sample increases as the effective stress increases. This relationship is consistent with the results in Panel A because as the effective stress increases, the volume of liquefaction will decrease. However, the same relationship between effective stress and Young's Modulus is not observed with variations in the lacustrine deposit Young's Modulus. There, the volume of liquefaction increases as the lacustrine Young's Modulus increases. The increase in fluid pressure within the lacustrine deposit may account for the discrepancy with the literature trends because an increase in pore fluid content will decrease the Young's Modulus, and wet and dry samples behave differently under triaxial tests (Rybacki, et al., 2015).

The volume of liquefaction decreases as the glacial till Poisson's Ratio increases in Figure 6 Panel B. Larger values of Poisson's Ratio indicate that there will be more strain (or displacement) in the direction perpendicular to the applied force during a triaxial test. A larger Poisson's Ratio in this case may indicate that the material accommodates some of the force from an increase in pore pressure, which could maintain some grain-to-grain contact and increase the effective stress relative to a small Poisson's Ratio. Then, the increase in effective stress would result in a decrease in the volume of liquefaction.

As the density of the lacustrine deposit and glacial till increases, the volume of liquefaction decreases in Figure 6 Panel C. An increase in material density will increase the weight of the material, and therefore the force that is applied to the material below a certain depth. As the force increases, the stress will increase. This will also increase the effective stress, which would require an increase in fluid pressure to reach a liquified condition. Variations in the lacustrine deposit density result in large changes in the volume of liquefaction compared to all other parameters. Therefore, the model is extremely sensitive to changes in the lacustrine density, which provides insight into the conditions required for soap hole formation.

In Figure 6 Panel D, the volume of liquefaction increases as the glacial till Biot-Willis Coefficient increases. As the glacial till Biot-Willis coefficient increases, the effective stress within the glacial till becomes more reliant on the fluid pressure. As the pore pressure increases around the fracture and the lacustrine-glacial till interface, the glacial till near the fracture and interface experiences a drop in effective stress as the Biot-Willis Coefficient increases. The volume of liquefaction then extends down past the lacustrine-glacial till interface into the glacial till.

The volume of liquefaction decreases as the thickness of the lacustrine deposit and glacial till increases in Figure 7 Panel A, although the change for the glacial till thickness is more significant. As the thickness of the units increases, there is a larger volume of material for the fluid pressure to disperse to, and less of the fluid pressure is concentrated within the lacustrine deposit. Above glacial till thicknesses of 30 m, there is no longer any liquefaction which suggests that an aquifer less than 30 m depth is required for soap hole formation.

In Figure 7 Panel B, the volume of liquefaction increases as the fracture width increases. A larger fracture results in a larger preferential flow path, which can translate more fluid pressure from the base of the model to the lacustrine-glacial till interface. The fluid pressure at the interface then increases resulting in a larger volume of liquefaction. A higher aquifer potentiometric surface also results in a larger volume of liquefaction due to a similar process (Figure 7 Panel C). A larger potentiometric surface results in an increase in fluid pressure through the fracture, which increases the fluid pressure at the lacustrine-glacial till interface and within the lacustrine deposit. The increase in fluid pressure then decreases the effective stress, which increases the volume of liquefaction.

The hypotheses to test the conceptual model for soap hole formation were either supported or partially supported.

1. Darcy's Law and poroelastic theory can accurately approximate the observed field phenomena. This hypothesis is partially supported. While the governing equations did produce an effective stress that falls within the effective stress of the field sites, the model results did not reproduce the observed effective stress outside the soap hole or the hydraulic head measurements at the field sites. Given the initial assumptions of the model, the results are an acceptable approximation of the observed field phenomena. Heterogeneity and/or anisotropy would need to be added to reproduce the field observations.

2. The combination of high flow path permeability and low lacustrine deposit permeability are essential to soap hole formation. This hypothesis is partially supported. A preferential flow path with a confining layer is essential to soap hole formation, but the relative hydraulic conductivities play less of a role.

3. Changes in elastic parameters will change the effective stress of the soil and soap hole formation. This hypothesis is supported. Variations in Young's Modulus, Poisson's Ratio, density, and the Biot-Willis Coefficient resulted in changes in the volume of liquefaction, which an effective stress less than or equal to zero as a proxy for liquefaction.

4. A flow path with high transmissivity will result in a more developed soap hole. This hypothesis is supported. A flow path with high transmissivity occurs when the hydraulic conductivity of the fracture is high and/or with a large fracture width. Both scenarios result with a larger volume of liquefaction.

5. The thickness of the lacustrine deposit and glacial till above the pressurized aquifer will affect the extent of liquefaction and soap hole formation. This hypothesis is supported. The lacustrine deposit thickness has a minor effect on the volume of liquefaction compared to the glacial till thickness. An increase in either unit's thickness results in a decrease in the volume of liquefaction.

CONCLUSIONS

This study focuses on the physical processes for soap hole formation. The hypotheses that are tested in this study support the conceptual model for soap hole formation developed by Woods (2019). Increased fluid pressure within the confining lacustrine deposit results in a decrease in effective stress and soap hole formation. The volume of liquefaction is sensitive to variations in hydraulic, elastic, and geometric parameters assigned to the model. Future work includes incorporating heterogeneity and/or anisotropy to the model units and including temporal variations to reproduce the seasonal variability of soap holes observed in the field data.

ACKNOWLEDGEMENTS

We thank the sponsors of CREWES for their continued support. This work was funded by CREWES industrial sponsors, NSERC (Natural Science and Engineering Research Council of Canada) through thee grant CRDPJ 543578-19, and NSERC Discovery Grant funds to Lauer.

REFERENCES

Burgess, N., & Eisenstein, Z. (1977). The application of pressuremeter test results in deformation analysis. Canadian Geotechnical Journal.

Carsel, R. F., & Parrish, R. S. (1988). Developing Joint Probability Distributions of Soil Water Retention Characteristics. Water Resources Research, 755-769.

Casey, B., Germain, J. T., Abdulhadi, N. O., Kontopoulos, N. S., & Jones, C. A. (2016). Undrained Young's Modulus of Fines-Grained Soils. 142(2).

COMSOL. (1998-2019). Reference Manual. COMSOL Multiphysics.

Cunningham, D. (In progress). Master of Science Thesis. Calgary, AB: University of Calgary.

Eisenstein, Z., & Morrison, N. A. (1972). Prediction of Foundation Deformations in Edmonton Using and In Situ Pressure Probe. Canadian Geotechnical Journal.

Eisenstein, Z., & Thomson, S. (1977). Geotechnical performance of a tunnel in till. Canadian Geotechnical Journal, 332-345.

Elwood, D., & Martin, C. D. (2010). Estimating soil properties using deformations associated with deep excavations. Proceedings of the 63rd Annual Canadian Geotechnical Conference and the 6th Canadian Permafrost Conference. Calgary, AB.

Grisak, G. E., & Cherry, J. A. (1975). Hydrologic Characteristics and Response of Fractured Till and Clay Confining a Shallow Aquifer. Canadian Geotechnical Journal.

Hamilton, A. B. (1966). Freezing shrinkage in compacted clays. Canadian Geotechnical Journal.

Hicher, P.-Y. (1996). Elastic Properties of Soils. 122(8).

Jalilzadeh, H. (2019). Field Performance and Water balance Predictions of Evapotranspirative Landfill Biocovers (Unpublished master's thesis). Calgary, AB: University of Calgary.

Knappet, J., Craig, R. F. (2020). Craig's Soil Mechanics 9e. CRC Press Taylor & Francis Group.

Krebes, E. S. (2019). Seismic Wave Theory. Cambridge University Press.

Morgan, L. R. (2019). Land use effects on groundwater recharge in the prairies (Unpublished master's thesis). Calgary, AB: University of Calgary.

Rybacki, E., Reinicke, A., Meier, T., Makasi, M., & Dresen, G. (2015). What controls the mechanical properties of shale rocks? - Part I: Strength and Young's modulus. 135.

Shatar, N. M. (2020). A Soap Hole Analysis by Cone Penetration Test (Unpublished undergraduate thesis). Calgary, AB: University of Calgary.

Toth, J. (1966). Mapping and interpretation of field phenomena for groundwater reconnaissance in a prairie environment, Alberta, Canada. Hydrological Sciences Journal, 20-68.

Toth, J. (1971). Groundwater discharge: a common generator of diverse geologic and morphologic phenomena. Hydrological Sciences Journal, 7-24.

van Genuchten, M. T. (1980). A closed-form equations for predicting the hydraulic conductivity of unsaturated soils. Soil Science Society of America Journal, 892-898.

Wang, H. (2000). Theory of Linear Poroelasticity with Applications to Geomechanics and Hydrogeology. Princeton University Press.

Wang, Z., Wong, R. C., Li, S., & Qiao, L. (2012). Finite element analysis of long-term surface settlement above a shallow tunnel in soft ground. Tunnelling and Underground Space Technology, 85-92.

Woods, L. G. (2019). A Conceptual Model for the Development and Persistence of Soap Holes (Unique Prairie Groundwater Discharge Features) (Unpublished master's thesis). Calgary, AB: University of Calgary.

Wosten, J. H., & van Genuchten, M. T. (1988). Using Texture and Other Soil Properties to Predict the Unsaturated Soil Hydraulic Functions. Soil Science Society of America Journal, 1769-1770.